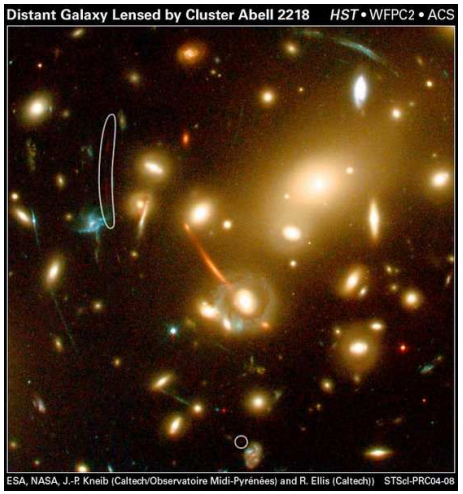

Probing the Dark Side of the Universe: Cosmology with Weak lensing Surveys

Dipak Munshi
Institute of Astronomy - University of Cambridge
Collaborators: P.Valageas, A.Barber, M.Kilbinger, L vanWaerbeke, A.Heavens

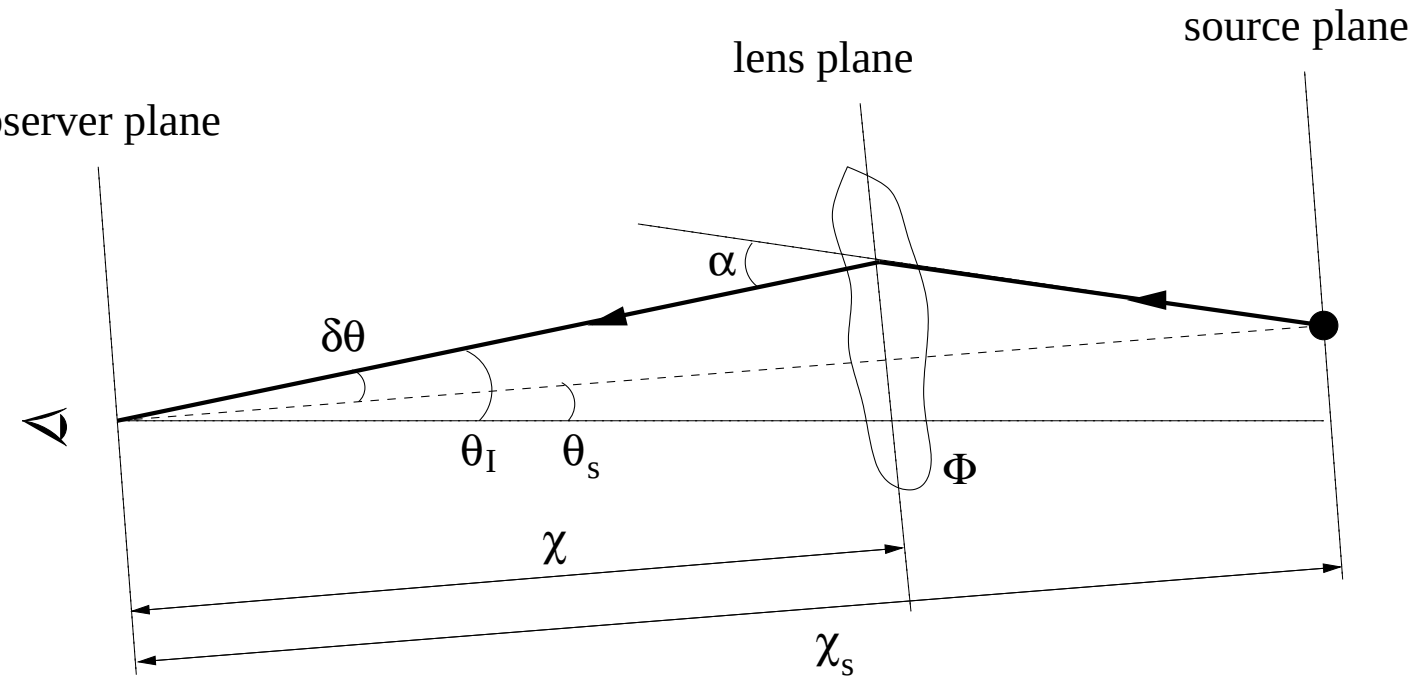

Figure 1:

The deflections can be expressed as:

$$\delta\vec{\theta} = \vec{\theta}_I - \vec{\theta}_s = \frac{2}{c^2}\int_0^{\chi_s} \mathrm{d}\chi\, \frac{\mathcal{D}(\chi_s - \chi)}{\mathcal{D}(\chi_s)}\, \nabla_\perp \Phi(\chi), \tag{1}$$

The observables are not the displacements but the distortions induced by these defelctions.They are expressed in terms of the shear matrix:

$$\Psi_{ij} = \frac{\partial \delta\theta_i}{\partial \theta_{sj}} = \frac{2}{c^2} \int_0^{\chi_s} \mathrm{d}\chi \, \frac{\mathcal{D}(\chi)\mathcal{D}(\chi_s - \chi)}{\mathcal{D}(\chi_s)} \, \nabla_i \nabla_j \Phi(\chi), \tag{2}$$

The amplification matrix encodes the distortions of the images

$$\mathcal{A} = \frac{\partial \vec{\theta}_s}{\partial \vec{\theta}_I} = (\delta_{ij} + \Psi_{ij})^{-1} = \begin{pmatrix} 1 - \kappa - \gamma_1 & -\gamma_2 \\ -\gamma_2 & 1 - \kappa + \gamma_1 \end{pmatrix}, \tag{3}$$

Radial Comoving Distance: χ Comoving Angular Diameter Distance: $\mathcal{D}$ Gravitational Potential: Φ

Convergence: κ Magnification: $1 + 2\kappa$ Shear: $\gamma = \gamma_1 + i\gamma_2$ Tangential Shear: γ_t, γ_+

Φ is linked to δ via Poisson Equation, so shear correaltion can directy be linked to matter Power Spectra

Many Aprroximations are involved e.g. Born Approximation in all analytical derivations

The lensing potential can be defined as $\phi(\vec{\theta}, \chi)$

$$\phi(\vec{\theta}, \chi) = \frac{2}{c^2} \int_0^{\chi_s} \mathrm{d}\chi \, \frac{\mathcal{D}(\chi_s - \chi)}{\mathcal{D}(\chi_s)\mathcal{D}(\chi)} \Phi(\chi, \mathcal{D}(\chi)\vec{\theta}), \tag{4}$$

The shear γ, convergence κ are related to the lensing potential

$$\gamma(\vec{l}) = -\frac{1}{2}(l_x + l_y)^2 \phi(\vec{l}) = \frac{l_x^2 - l_y^2 + 2il_x l_y}{(l_x^2 + l_y^2)} \kappa(\vec{l}) = exp(2i\alpha)\kappa(\vec{l}); \quad \vec{l} = (l_x, l_y) \tag{5}$$

Or these relations can be also written as:

$$\kappa = \frac{1}{2}(\partial_x^2 + \partial_y^2)\phi \quad \gamma_1 = \frac{1}{2}(\partial_x^2 - \partial_y^2)\phi \quad \gamma_2 = \partial_x \partial_y \phi \tag{6}$$

These relations are valid for Unsmoothed shear and convergence

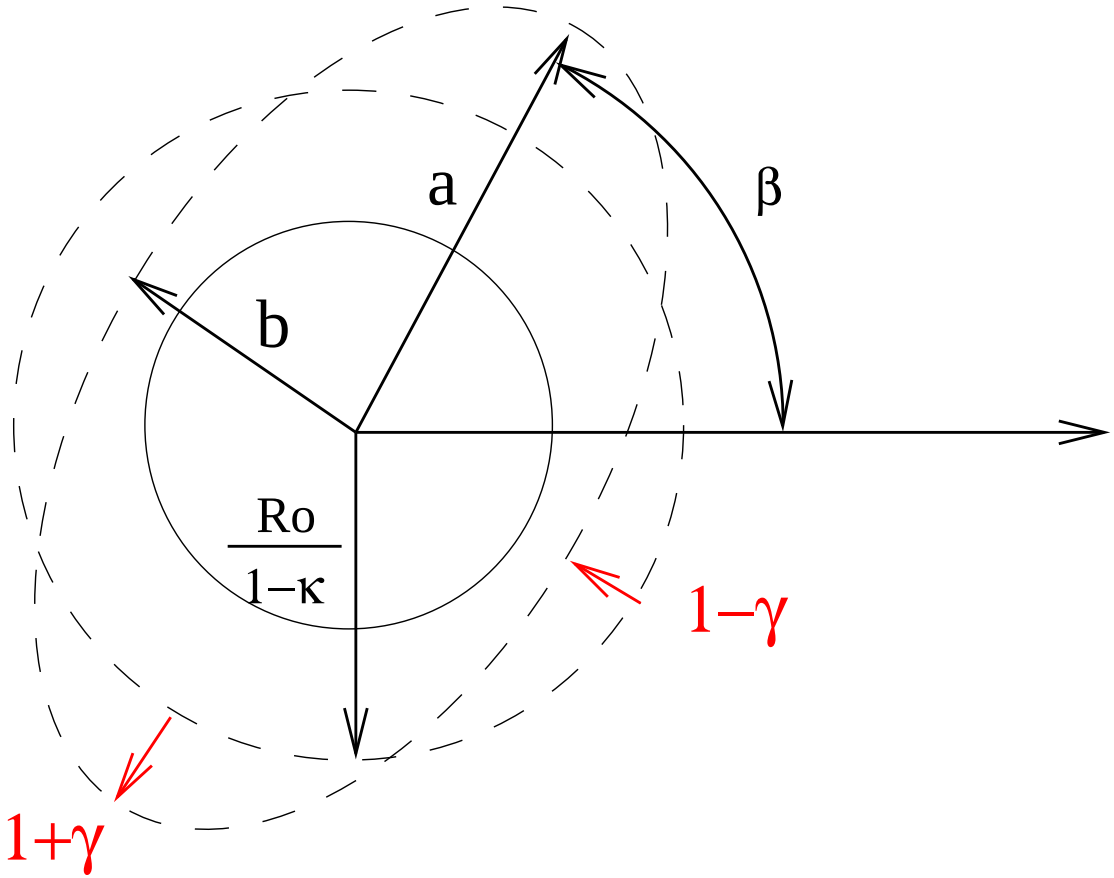

Figure 2:

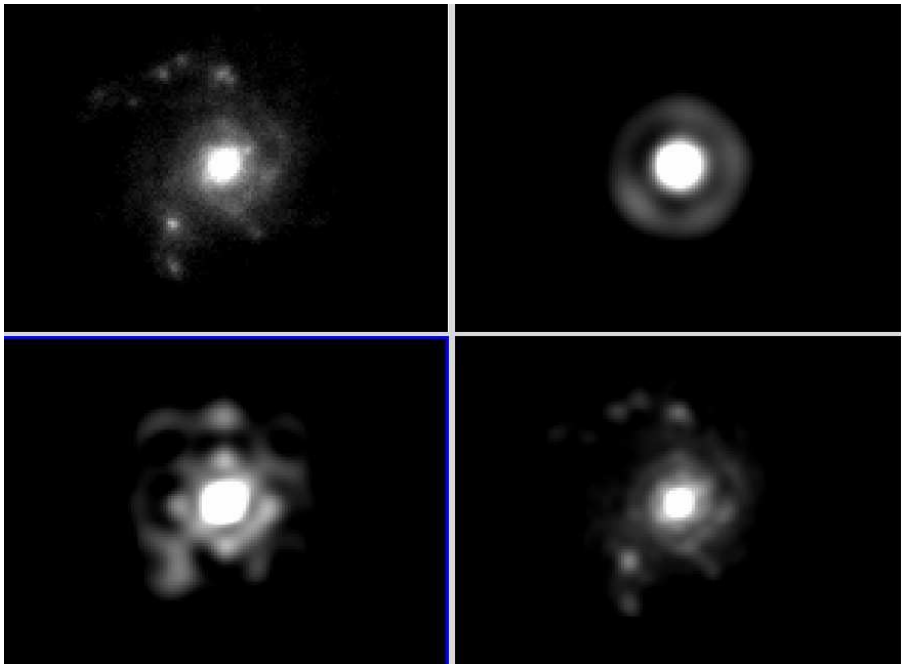

Figure 3: Higher order contributions to the Deflections can be quantified with Shapelets.

For Various -smoothed- estimators:

$$X(l) = W_x(-l\vec{\theta}_s)\kappa(l) \tag{7}$$

In real space this can be expressed as:

$$W_x(l\vec{\theta}_s) = \int d\vec{\theta}\exp(i\vec{l}.\vec{\theta})U_x(\vec{\theta}) \tag{8}$$

$$W_\kappa = \frac{2J_1(l\theta_s)}{l\theta_s} \quad W_\gamma(l\theta) = W_\kappa(l\theta)Exp(i2\alpha) \tag{9}$$

These expressions can be employed to reconstruct the projected mass distributions.

In almost all analytical expressions the approximations that are used are listed below:

- Sorce and Lens Coupling
- Weak vs Strong Lensing for high convergence regions
- Source density fluctuations
- Born Approximation

This is where Numerical Simulations are useful

- Line of Sight Integration
- Ray Tracing Experiments

Evolution of projected Power Sepectrum

- Weak Lensing gives unbiased probe of nonlinear matter PS.
- It can probe variation of of PS for a range of angular scales as a function of redshift z
- Systematics need to be controled extremely well at a few percent accuracy.

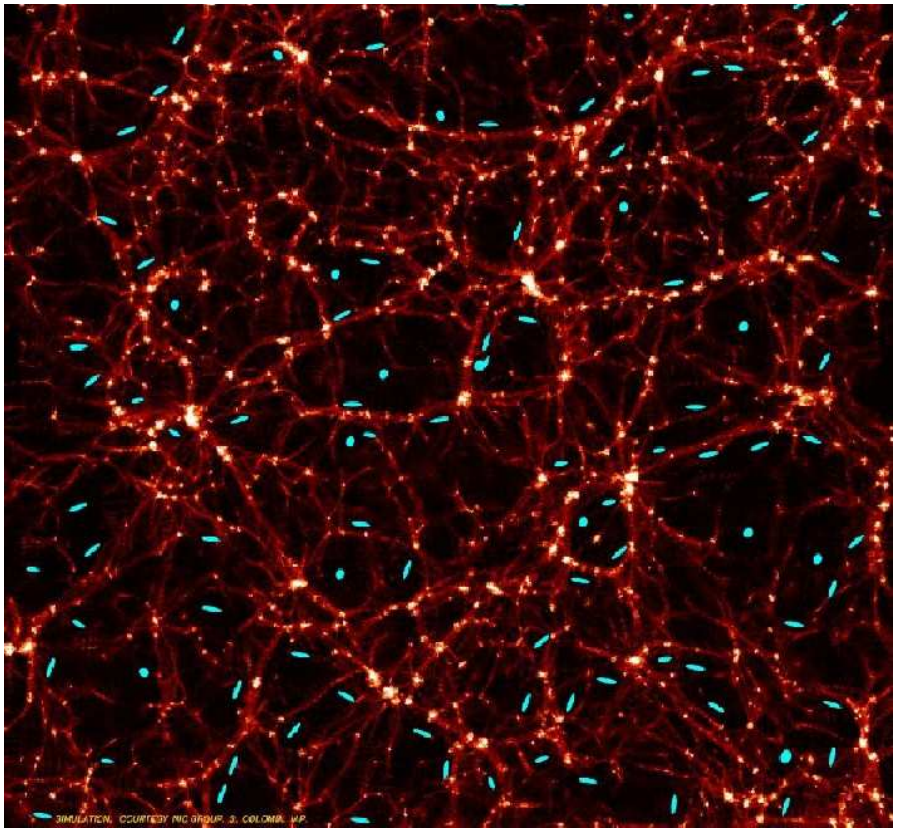

Figure 4: Highly magnified alignment of lensed galaxies is shown superposed on the projected cosmic wabe.Figure Courtesy: S. Colombi.

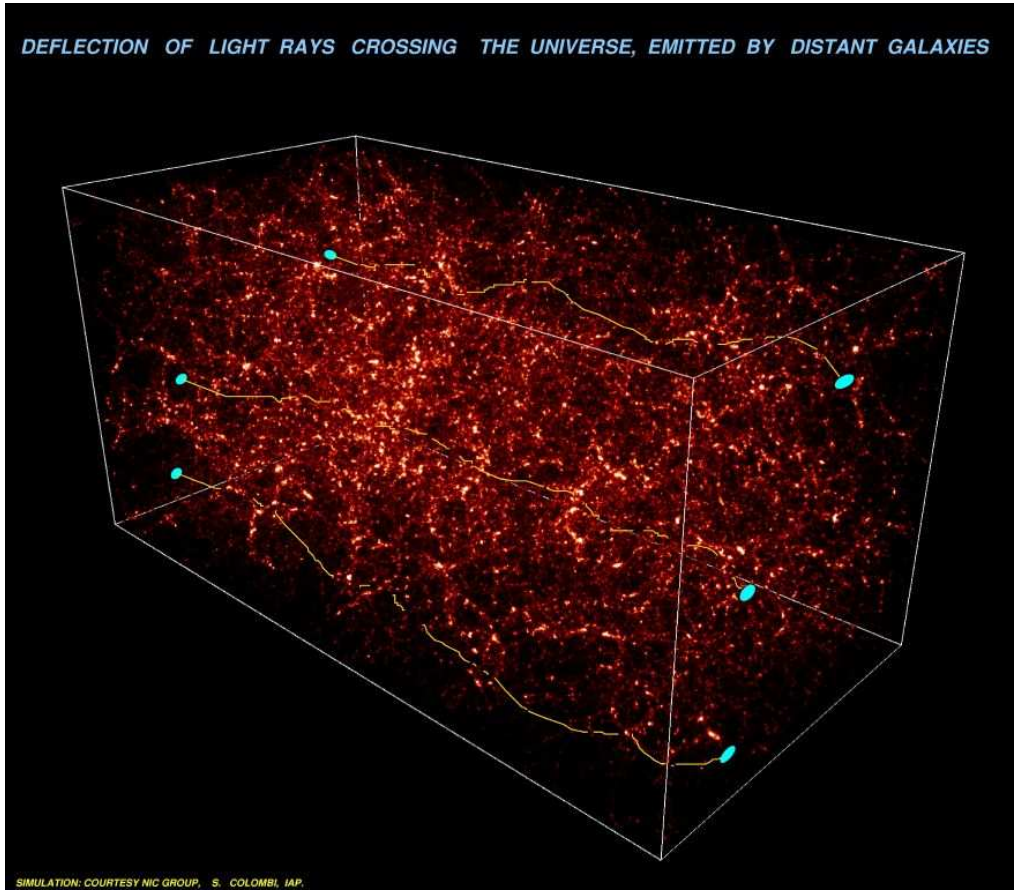

Figure 5: Results of a raytracing experiment is shown along with the mass distribution. The source redshift is unity. Figure Courtesy: S. Colombi.

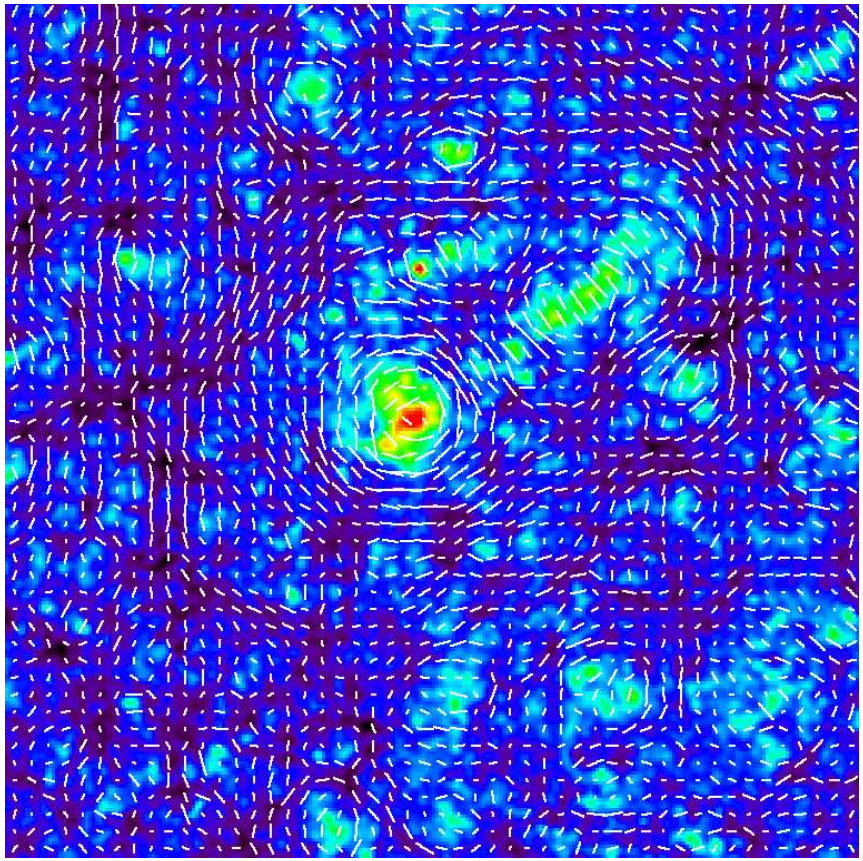

Figure 6: Highly magnified alignment of lensed galaxies is shown superposed on the projected cosmic wabe.Figure Courtesy:Various

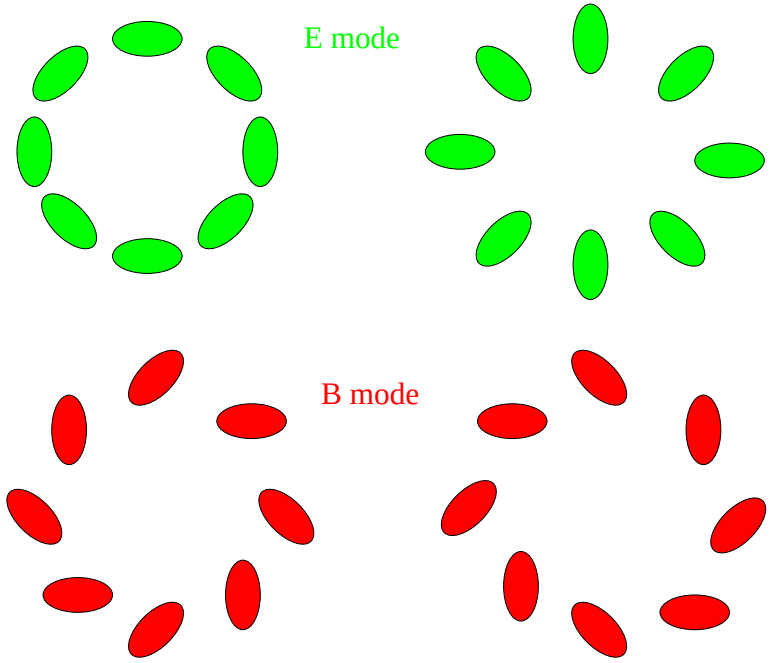

Figure 7: E and B mode decomposition: E is important and B is -mostly- systematic. The left panel depicts shear pattern around overdense regions and the right panels shows the same for underdense regions.

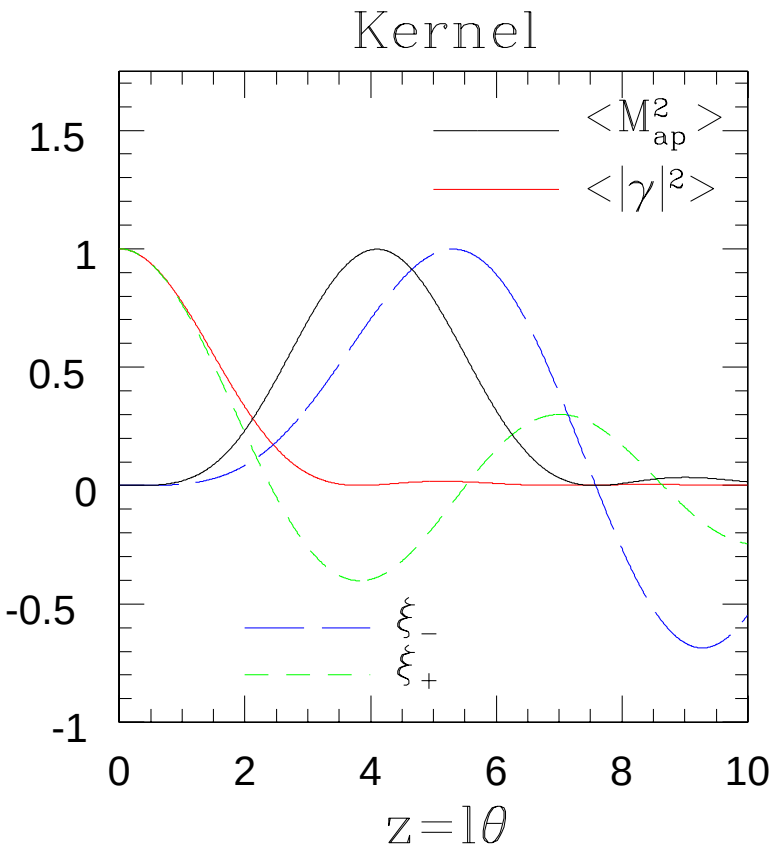

Figure 8:

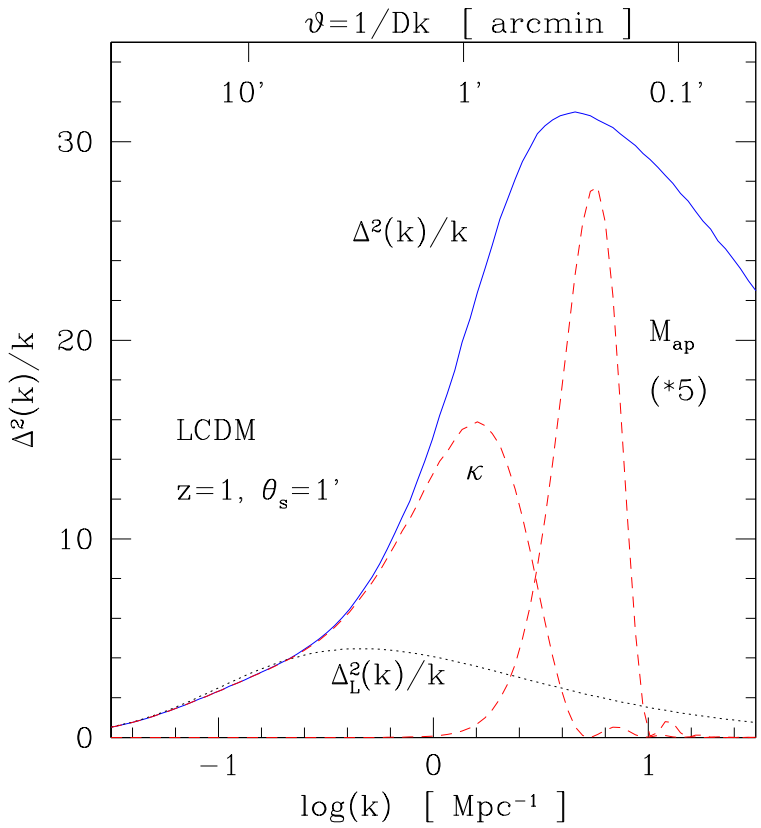
ϑ=1/Dk [arcmin]
10'
1'
0.1'
30
20
10
0
Δ²(k)/k
LCDM
z=1, θs=1'
Δ²(k)/k
κ
Map
(*5)
Δ²L(k)/k
−1
0
1
log(k) [Mpc⁻¹]

Figure 9:

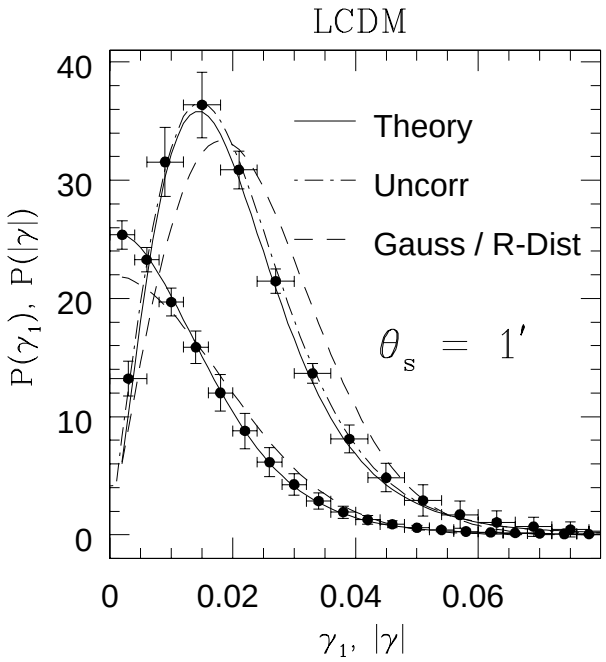

Figure 10:

Modelling of non_Gaussianity

- Weak Lensing probes nonlinear scales.
- It can provide additional constraints on LSS scenarios by providing information regarding gravity induced non-Gaussianity.

- Here we assume Hierarchical Model for evolution of non-Gaussianity.
- Again to achive all these the systematics need to be controled extremely well.

- Variation of $\langle \kappa_s^2 \rangle^{1/2}$ as a function of source redshift z_s is shown.
- Numerical simulations use LINE of SIGHT INTEGRATION and NOT ray tracings.
- The error bars are the scatter from 20 realisations of the same simulations so are NOT completely independent.

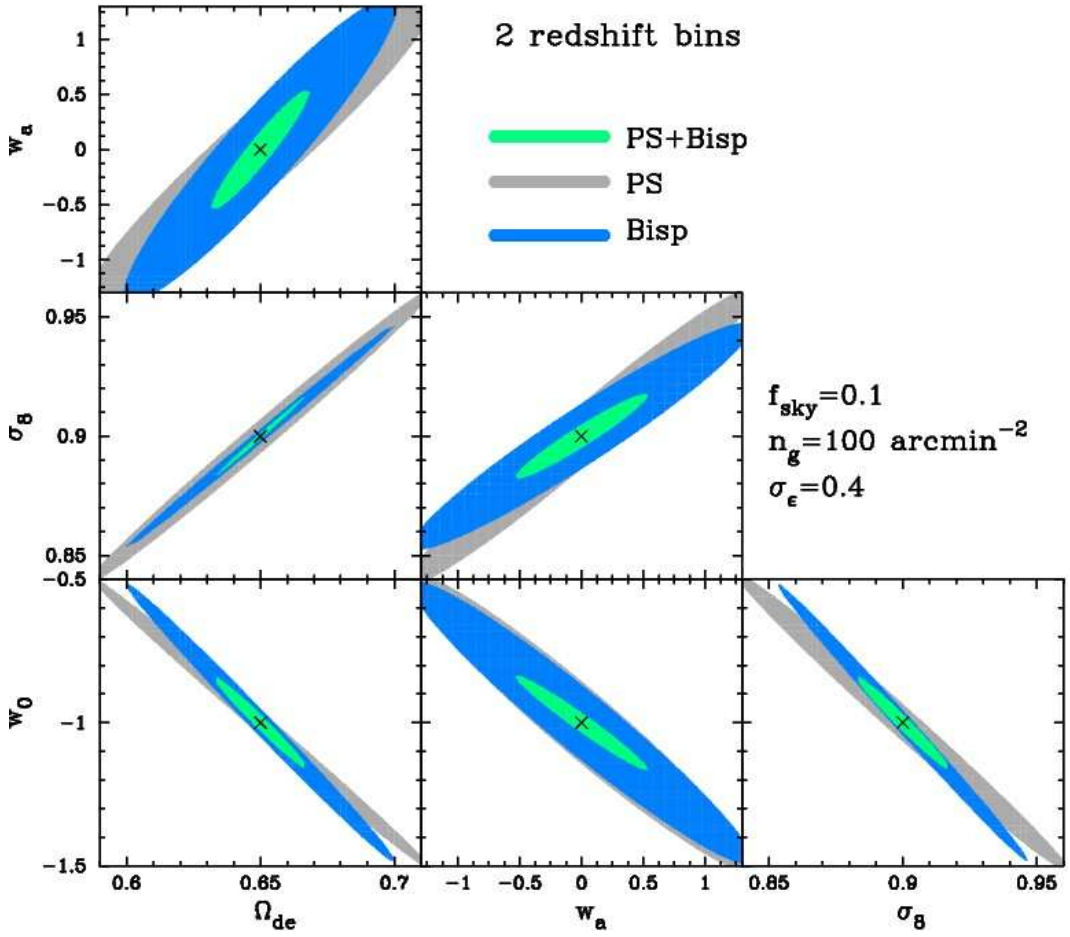

Figure 11: Projected 68% confidence level constraints in the parameter space of $\Omega_{\rm de}$, w_0, w_a and σ_8 from the lensing power spectrum and the bispectrum in two redshift bins, as indicated. The coefficients w_0 and w_a parameterize the equation of state of the dark energy component. The results shown are obtained assuming priors on n, $\Omega_{\rm b}h^2$ and h expected from the Planck mission. The sky coverage and number density are taken to be $f_{\rm sky}=0.1$ and $n_g=100$ arcmin^{-2}, and angular modes $50\le l\le 3000$ are used. From Takada & Jain (2004).

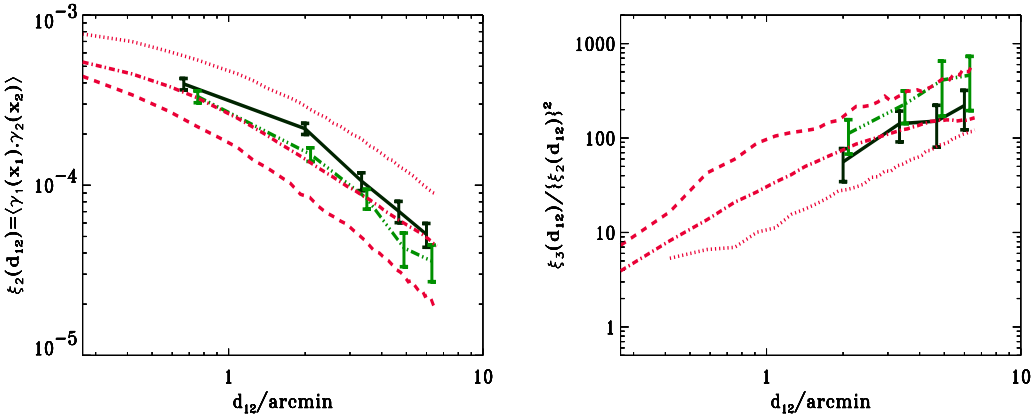

Figure 12: Results for the VIRMOS-DESCART survey for the two point correlation function (left) and the reduced three point function (right). The solid line with error bars shows the raw results, when both the E and B contributions to the two-point correlation functions are included. The dot-dashed line with error bars corresponds to measurements where the contribution of the B mode has been subtracted out from the two-point correlation function (but not from ξ_3 there is no known way to do it). These measurements are compared to results obtained in τCDM, OCDM and ΛCDM simulations (dashed, dotted and dot-dashed lines respectively). From Bernardeau et al. (2002).

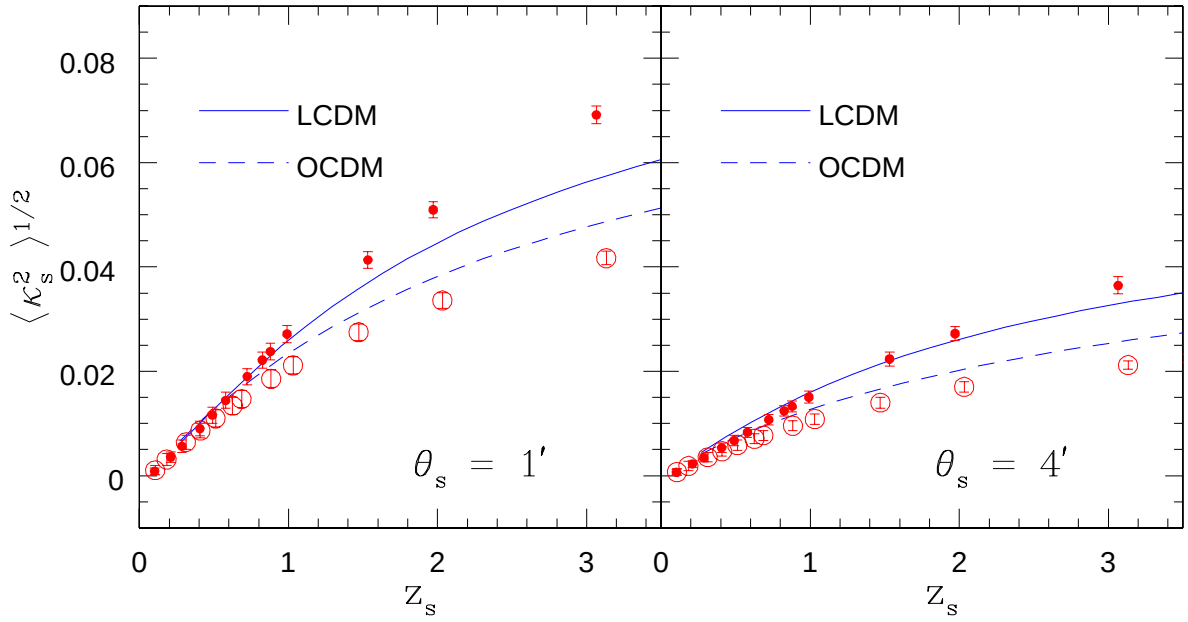
0.08
0.06
0.04
0.02
0
$\langle \kappa_s^2 \rangle^{1/2}$
LCDM
OCDM
$\theta_s = 1'$
0
1
2
3
z_s
LCDM
OCDM
$\theta_s = 4'$
0
1
2
3
z_s

Figure 13:

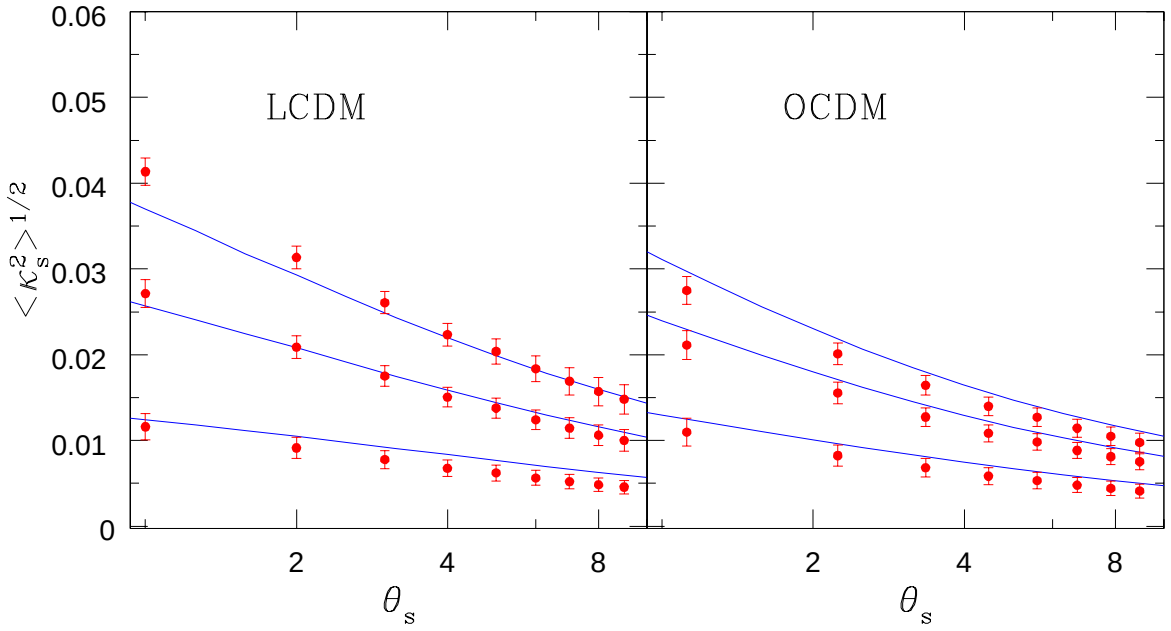

Figure 14:

- Variation of $\langle\kappa_s^2\rangle^{1/2}$ as a function of smoothing angluar scale θ_s is shown.
- Curves from top to bottom correspond to sources redshifts $z_s = 1.5, 1., .5$
- The signal is higher as we probe deeper.
- Box size is small and realisations are not completely independent

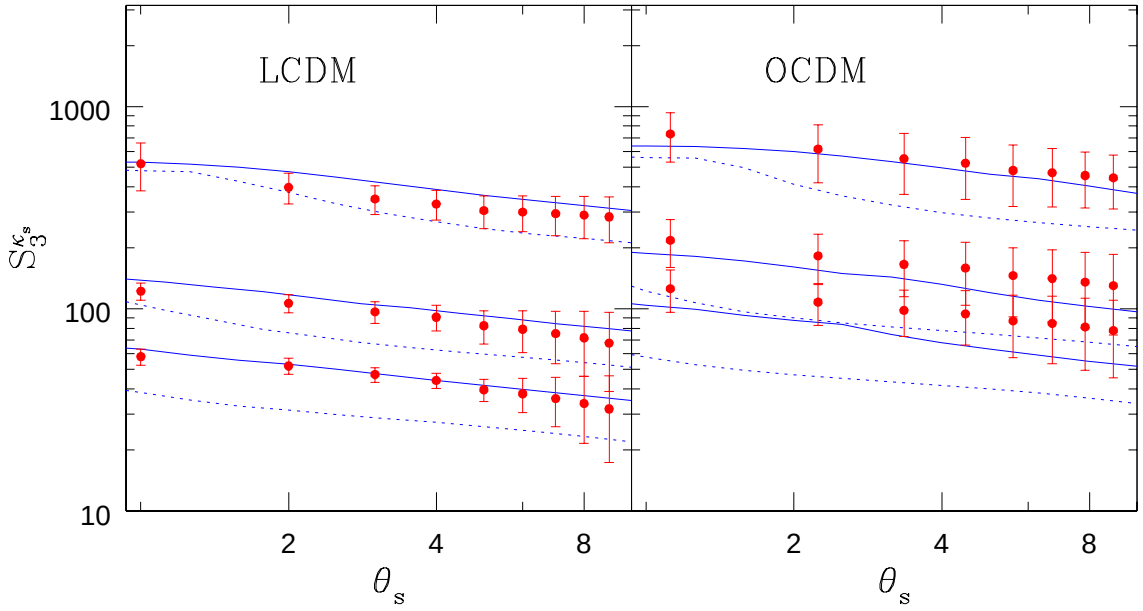

Figure 15:

- Variation of $\langle \kappa_s^2 \rangle^{1/2}$ as a function of smoothing angluar scale θ_s is shown.

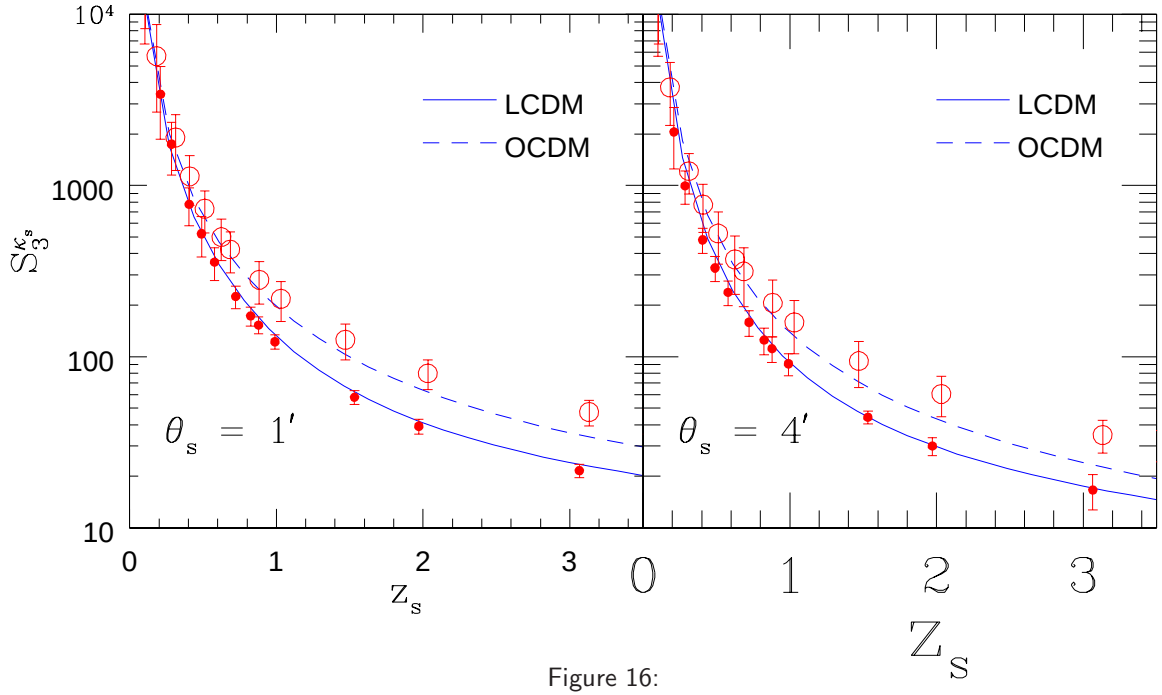

Figure 16:

Optimization of Survey Strategy - Real Space Analysis

Scatter can be decomposed into three dominant contributions

- Scatter due to finite survey size i.e. sampling variance.
- Scatter due to finite number of source galaxies within the survey area/volume.

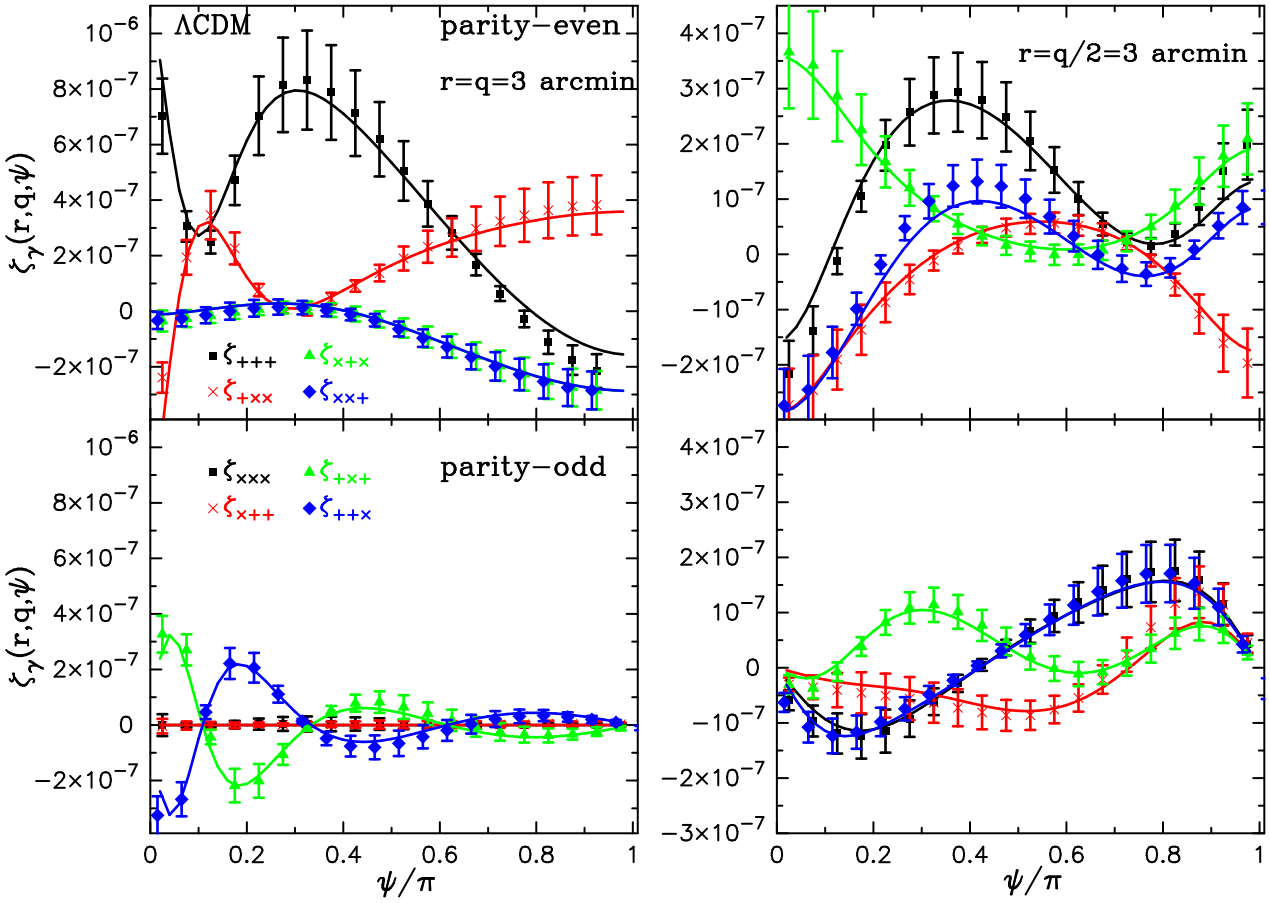
ΛCDM
parity−even
r=q=3 arcmin
r=q/2=3 arcmin
parity−odd
ζ_{+++}
ζ_{x+x}
ζ_{+xx}
ζ_{xx+}
ζ_{xxx}
ζ_{+x+}
ζ_{x++}
ζ_{++x}
$\zeta_\gamma(r,q,\psi)$
ψ/π

Figure 17:

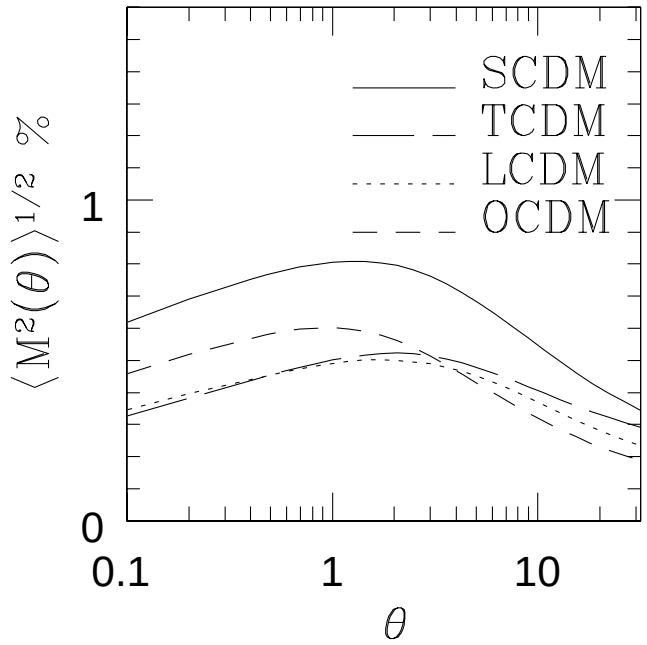

Figure 18:

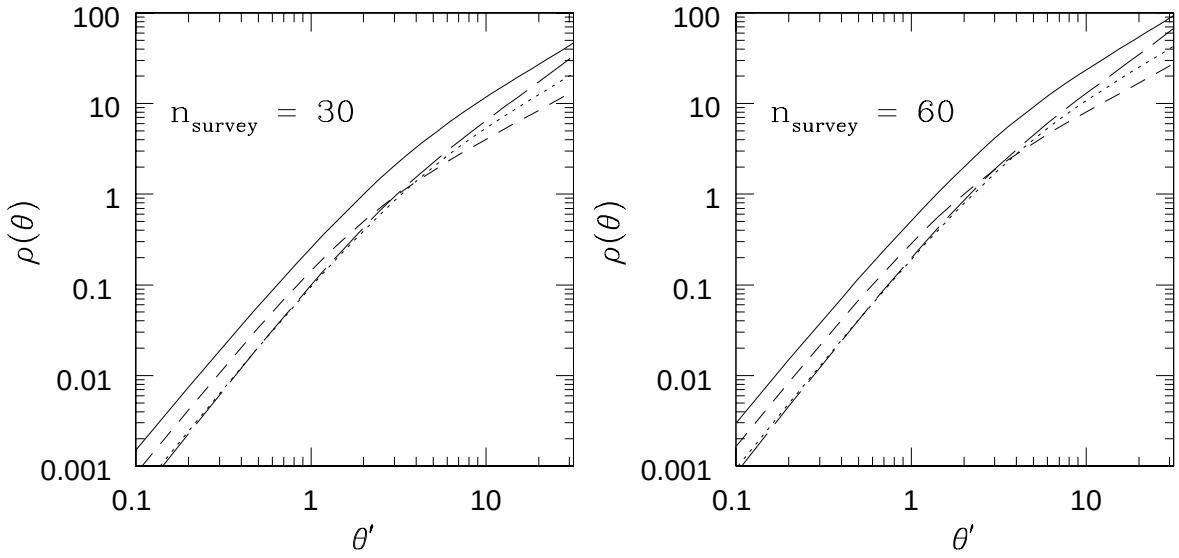

- Scatter due to intrinsic ellipticity distribution of source galaxies

- The quantity $\rho(\theta)$ is similar to projected source density
- It is shown as a function of the smoothing angular scale θ.
- $\rho(\theta)$ and is an important ingradient in expressions involving various contribution to scatter.
- Errors at various orders depend only on various powers of aperture mass, $\rho(\theta)$ and normalised one point moments.

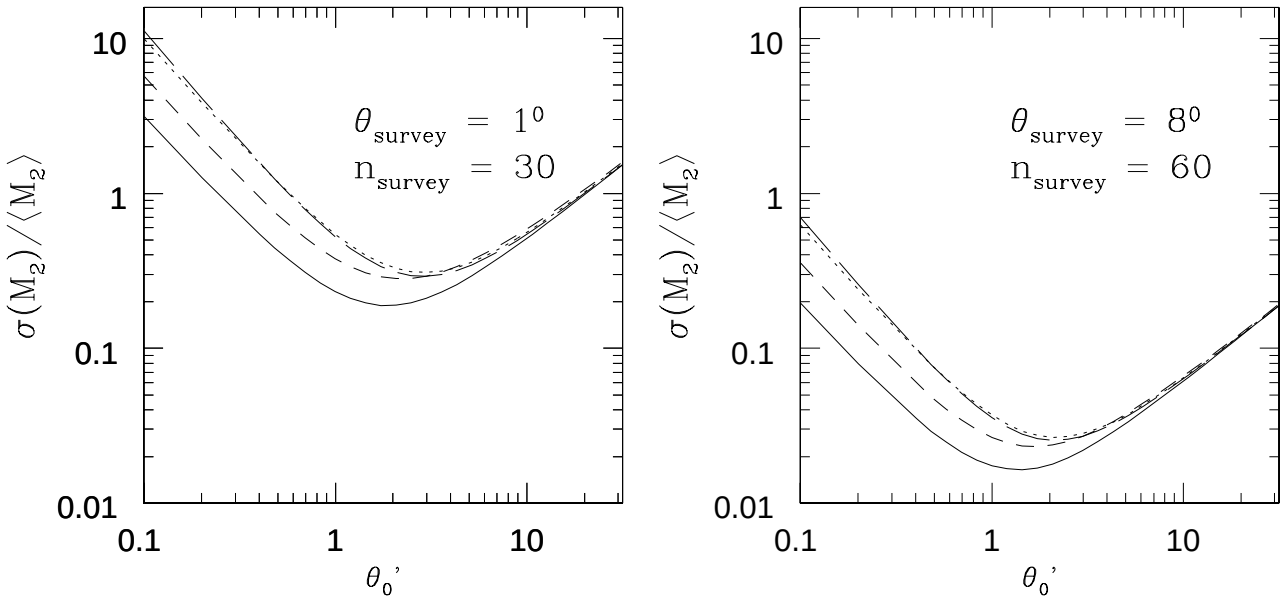

Figure 19:

- The error associated with estimation of M_{ap} is shown.
- The small angular scale error is dominated by shot noise and intrinsic ellipticity distribution error.
- The large angular scale is associated with sampling variance term and depends on the survey size
- The left panels correspond to a ground based survey while the right panel depicts results for space based observations.

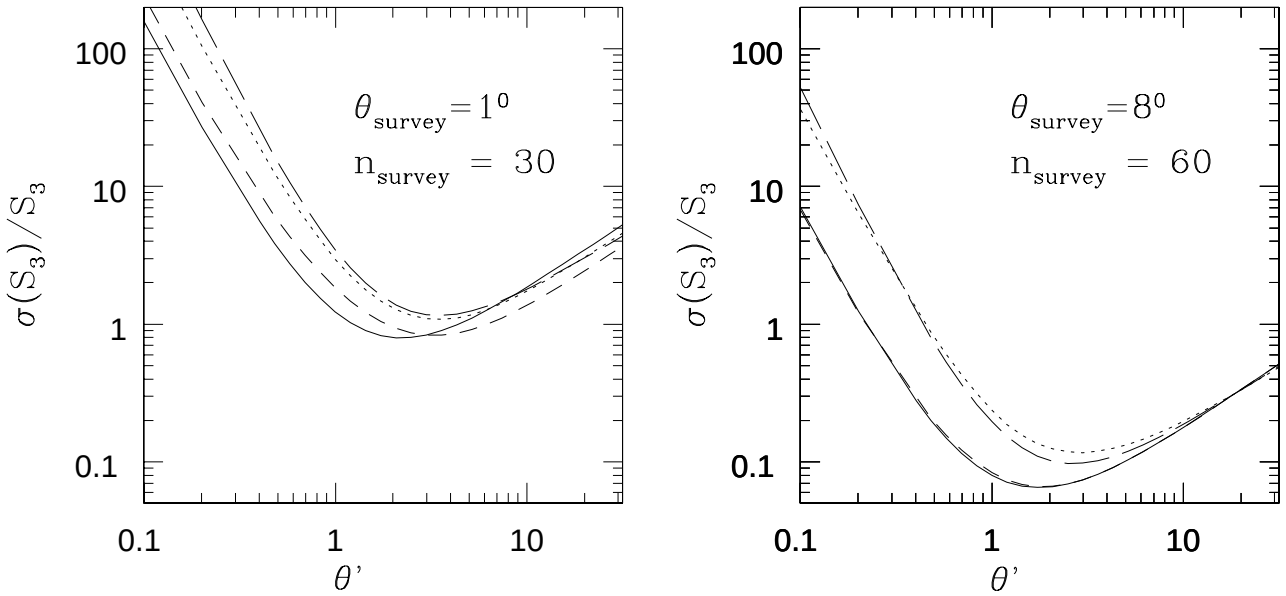

Figure 20:

- The scatter is higher at the level of three-point function.
- However the skewness can still be measured with few percent level accuracy for a range of angular scale which can be probed by space based observations.

This analysis depends on the local nature of Aperture Mass M_{ap}.
Simulations are needed to study the other windows $\xi_{\pm}$

Optimization of Survey Strategy - A Fisher Analysis

Real Space Estimators

The estimators $\xi_{\pm}(\theta)$, $\left\langle M_{\rm ap}^2(\theta)\right\rangle$ and the associated windows $\mathrm{J}_{0,4}(\ell\theta)$, $\mathrm{J}_4(\ell\theta)$ to the power specra are given by:

$$\begin{aligned}\xi_{\pm}(\theta) &= \frac{1}{2\pi}\int_0^\infty \mathrm{d}\ell\,\ell\,P_\kappa(\ell)\mathrm{J}_{0,4}(\ell\theta);\\ \left\langle M_{\rm ap}^2(\theta)\right\rangle &= \frac{1}{2\pi}\int_0^\infty \mathrm{d}\ell\,\ell\,P_\kappa(\ell)\left(\frac{24\,\mathrm{J}_4(\ell\theta)}{(\ell\theta)^2}\right)^2,\end{aligned} \tag{10}$$

Fisher's Analysis

Rough local estimates. Correct upto second order. Known to reproduce the degeneracy directions correctly.

$$F_{ij} = \sum_{ij}\left(\frac{\partial x_k}{\partial\Theta_i}\right)(\mathbf{C}^{-1})_{kl}\left(\frac{\partial x_l}{\partial\Theta_j}\right), \tag{11}$$

$$\mathbf{F}^{-1} = \langle\Delta\vec{\Theta}\Delta\vec{\Theta}^{\rm t}\rangle = \langle\vec{\Theta}\vec{\Theta}^{\rm t}\rangle - \langle\vec{\Theta}\rangle\langle\vec{\Theta}^{\rm t}\rangle. \tag{12}$$

Eigen Analysis or Principal Component Analysis

$$\mathbf{F} = \mathbf{W}^{\mathrm{t}} \mathbf{\Lambda} \mathbf{W}, \tag{13}$$

where $\mathbf{\Lambda}$ is a diagonal matrix. The quantities $\vec{\Phi} = \mathbf{W}\vec{\Theta}$ are uncorrelated because their covariance matrix is diagonal,

$$\langle \Delta\vec{\Phi} \Delta\vec{\Phi}^{\mathrm{t}} \rangle = \mathbf{W} \langle \Delta\vec{\Theta} \Delta\vec{\Theta}^{\mathrm{t}} \rangle \mathbf{W}^{\mathrm{t}} = \mathbf{\Lambda}^{-1}. \tag{14}$$

By multiplying $\mathbf{W}$ with the square root of the diagonal matrix $\mathbf{\Lambda}$.
The quantities $\vec{\Phi}$ can be scaled to unit variance without loss of generality. In this case, (13) is written as

$$\mathbf{F} = \tilde{\mathbf{W}}^{\mathrm{t}} \tilde{\mathbf{W}}, \tag{15}$$

Here we have defined: $\tilde{\mathbf{W}} = \mathbf{\Lambda}^{1/2}\,\mathbf{W}$.

$$\Delta\Theta = \left(\sum_{j=1}^{n} W_{ji}^2 \lambda_i^{-1} \right)^{1/2} \tag{16}$$

Most often the first few eigen modes are sufficient to compress all the information regarding the scatter.

Modelling the Source Distributions

$$p(z)\mathrm{d}z = \frac{\beta}{z_0\Gamma(3/\beta)}\left(\frac{z}{z_0}\right)^2 e^{-(z/z_0)^\beta}\mathrm{d}z, \tag{17}$$

- Fiducial values for $z_0 = 1$ and $\beta = 1.5$.hroughout, the intrinsic ellipticity dispersion is set to $\sigma_\epsilon = 0.3$.
- The number of galaxies per square arc minute, for which a shape mesurement is feasible, is set to 30.

Simulating the Survey

- The individual images are 13 arc-minutes by 13 arc-minutes. This correspond to field of view of VMOS.
- A survey consists of P patches of Radius R which contains N images.
- The total number of images is fixed but N and R can be changed.

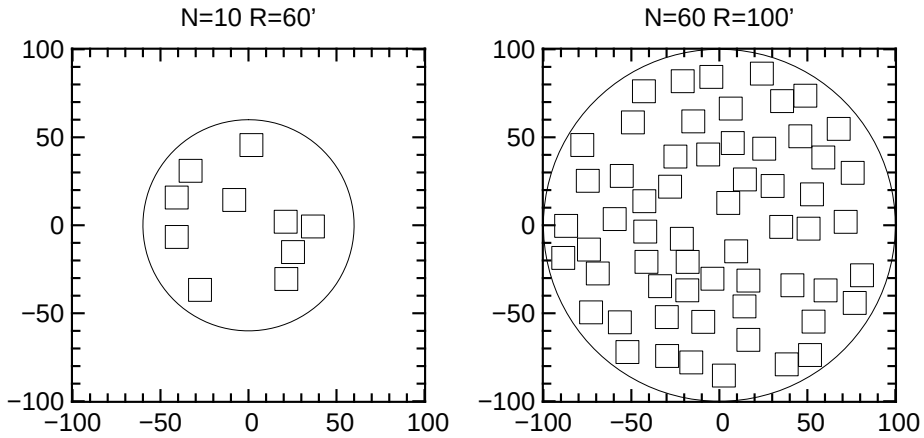
N=10 R=60’
N=60 R=100’
100
50
0
−50
−100
−100
−50
0
50
100

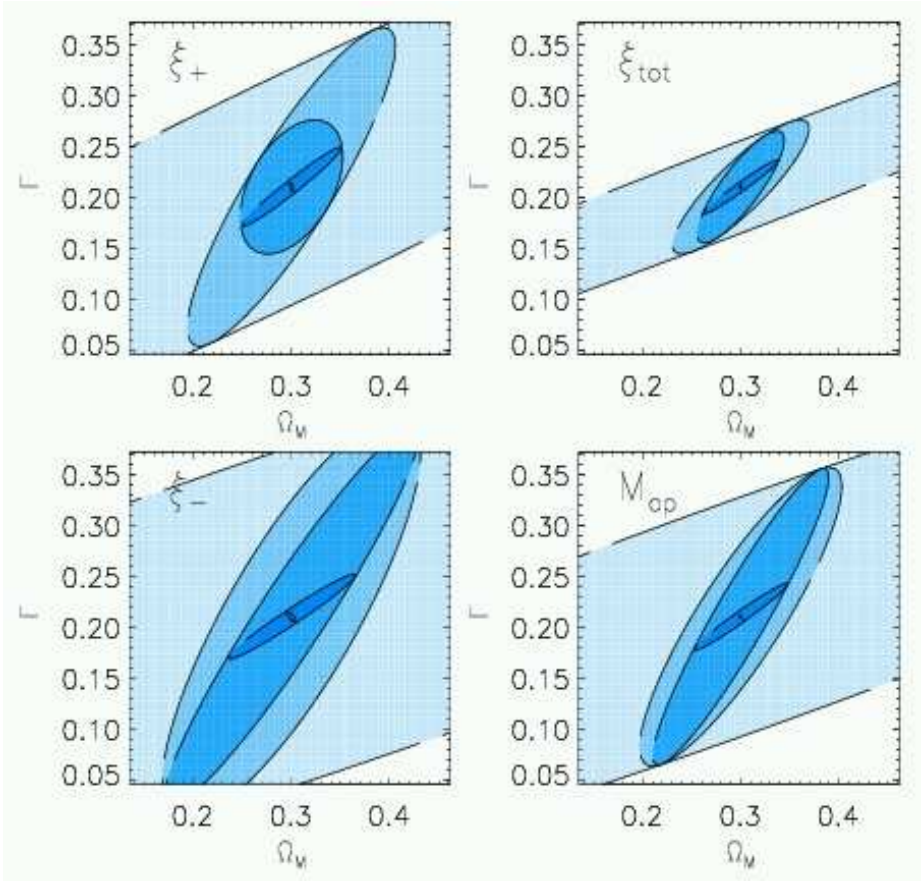

Figure 21: σ error ellipses in the Ω_m-Γ plane. From small to large ellipses, successive marginalisation over $\sigma_8, n_{\rm s}, \Omega_\Lambda, \beta, z_0$ (except the ones that are plotted) was performed. The four panels correspond to the four estimators ξ_+, ξ_-, $\xi_{\rm tot}$ and $\langle M_{\rm ap}^2 \rangle$ as indicated. $\xi_\pm = \xi_{tt} \pm \xi_{xx}$.

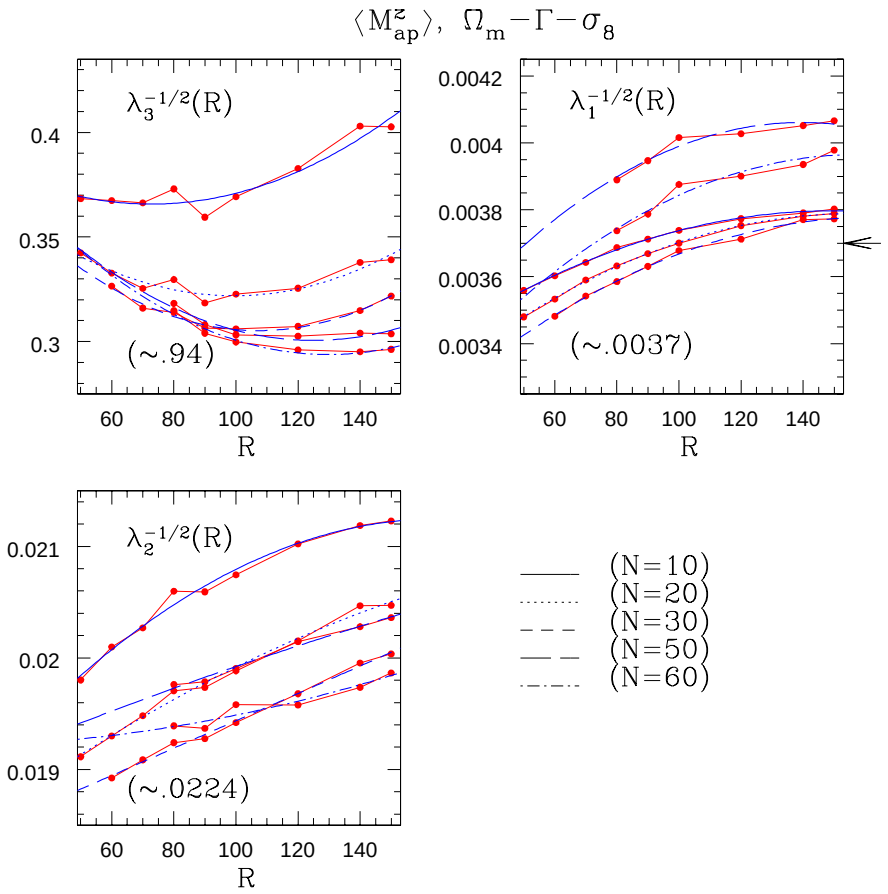

Figure 22: The variance $\sigma_i = \lambda_i^{-1/2}$ of the three eigenvectors of the Fisher matrix $\mathbf{F}$, corresponding to (Ω_m, Γ, σ_8) and a flat Universe, for $\langle M_{\rm ap}^2 \rangle$. Various surveys (N, R) are being compared. The results for the $300 \cdot 13'^2$ survey is written in brackets in each panel and, while within the range of the plot, marked with an arrow. The smooth curves are second-order polynomial fits to the data points.

Tomography and 3D Maps

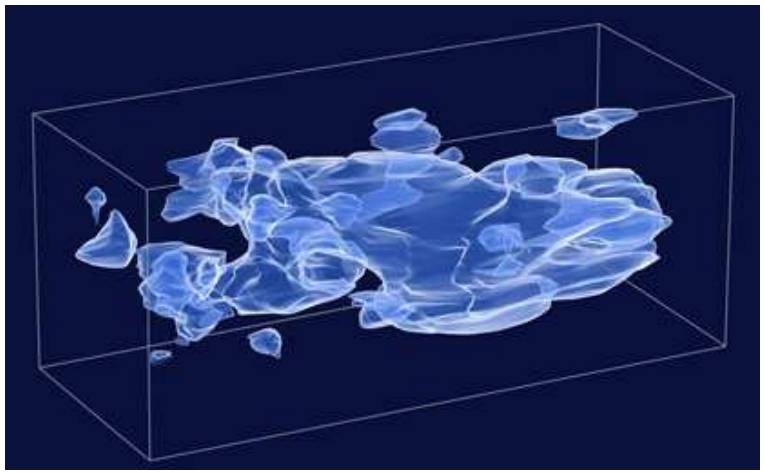

- It is possible to de-project the map and the ps with redshift information.
- In principle it would be ideal to have spectroscopic redshift of each galaxies.
- However it is much easier to simply bin them in few photometric bins.
- The intrinsic aligments of the galaxies due to tidal gravitational fields also can be avoided if we use redshift information.

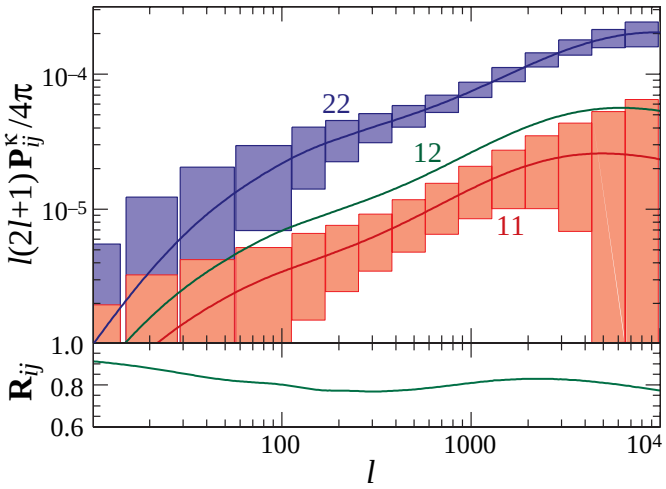

Figure 23: A plot explaining use of tomography in estimations of power spectrum in weak lensing surveys. Hu 1999.

- This increases the accuracy of estimated comological parameters.
- Fisher matrix based analysis indicates that having just 2-3 bins can improve the accuracy and having more bins will have marginal effects.
- A full 3D reconstruction of dark mass distribution too can be achived with accurate redshift information.
- The above image is based on Hubble observations of $3^\circ \times 3^\circ$ patch with redshift range covered from 0-1.

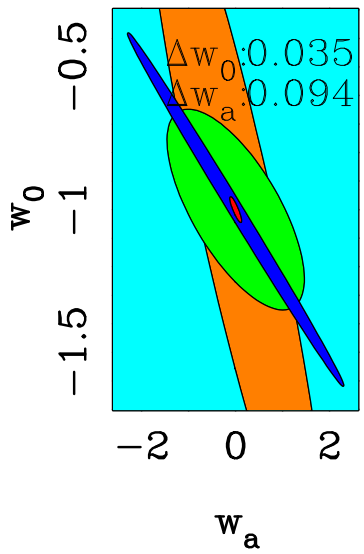

Figure 24: The accuracy expected from the combination of experiments dedicated to studying dark energy properties. The equation of state of dark energy is assumed to vary with scale factor a as $w(a) = w_0 + w_a(1-a)$, and the figures show the 1-sigma, 2-parameter regions for the experiments individually and in combination. The supernova study fills the plot, the thin diagonal band is Planck, the near-vertical band is BAO, and the ellipse is the 3D lensing power spectrum method. The small ellipse is the expected accuracy from the combined experiments. From Heavens et al. (2006).

Joint Analysis with Other Probes

The assumed experiments are: a 5-band 3D weak lensing survey, analysed either with the shear ratio test, or with the spectral method, covering 10,000 square degrees to a median redshift of 0.7, similar to the capabilities of a groundbased 4m-class survey with a several square degree field; the Planck CMB experiment (14-month mission); a spectroscopic survey to measure baryon oscillations (BAO) in the galaxy matter power spectrum, assuming constant bias, and covering 2000 square degrees to a median depth of unity, and a smaller $z = 3$ survey of 300 square degrees, similar to WFMOS capabilities on Subaru; a survey of 2000 Type Ia supernovae to $z = 1.5$, similar to SNAP's design capabilities.

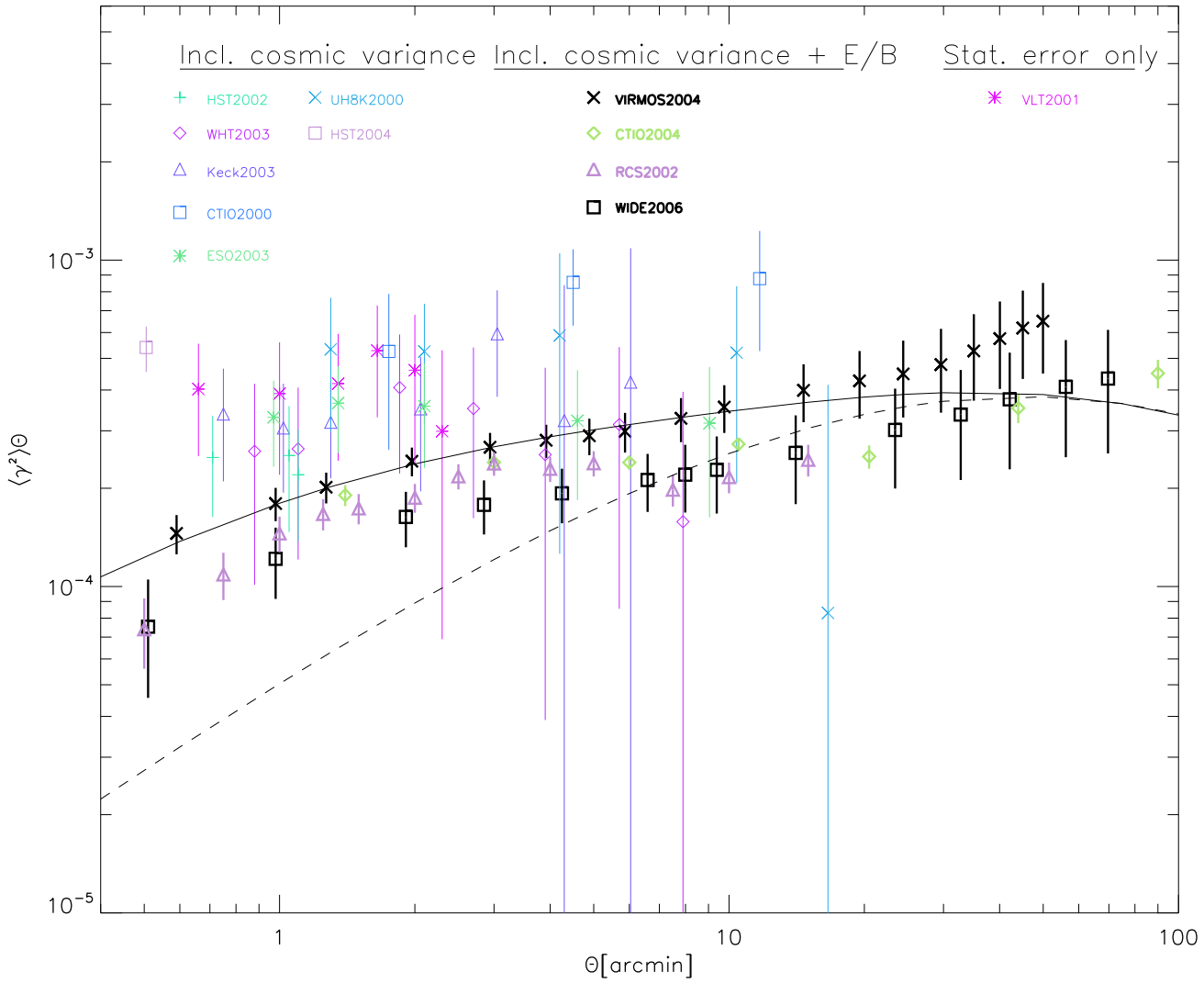
Incl. cosmic variance
Incl. cosmic variance + E/B
Stat. error only
HST2002
UH8K2000
VIRMOS2004
VLT2001
WHT2003
HST2004
CTIO2004
Keck2003
RCS2002
CTIO2000
WIDE2006
ESO2003
10^{-3}
10^{-4}
10^{-5}
$\langle\gamma^2\rangle_\Theta$
1
10
100
Θ[arcmin]

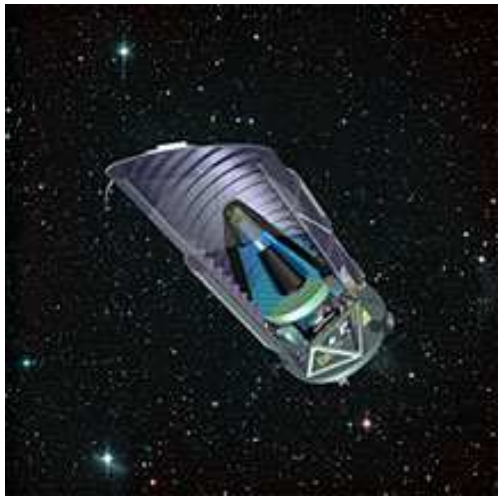

Figure 25: SNAP

SN surveys and the Effect of Weak Lensing

- SNIA are excellent tools for observational cosmology because of their low intrinsic scatter
- The are used to calibrate the redshift-distance relation and hence constrain cosmology.
- They too are affected by gravitational lensing. It increases the scatter as well as introducesa bias
- $z_s < .5$ there are no significant bias but for $z_s > 1$ the effect needs to be taken into account (e.g. for pencil beam survey)
- However the weak lensing of SN can also be exploited to extract useful cosmological information

- Being point sources only magnification is important rather than shear.

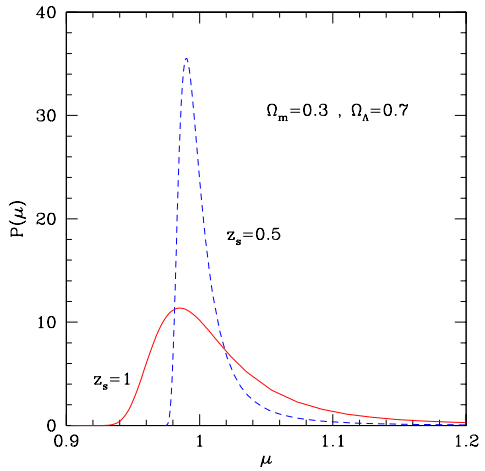

Figure 26: Probability Distribution of Magnification P(μ) as a function of μ.

- Weal Lensing modifies the observed ellipticities by less than 10% so many galaxies are needed to extract the signal. The magnification of a type 1A SN by wl is of the same order as its intrinsic magnitude dispersion so S/N is high.
- Since number of SN is smaller so the detection however is difficult.
- Nevertheless It has been suggested that the correaltion between SN1A magnitude and foreground galaxies can be used as a reconstruction probe for foreground galaxy overdensity

Summary and Outlook

- Adequate detectors are more important than larger telescopes.
- Wide field view is needed and well sampled PSF.
- The main reason for recent progress in weak lensing studies is because of advancement in CCD technology.

- The situation is somewhat similar to Pre-Cobe era.
- Largest Survey at present is CFHTLS.
- Next generation surveys will provide nearly full sky coverage.
- Transition from 1% accuracy level to sub-percent accuracy will be needed to analyse these future surveys
- Many "Unknown-unknowns" can compilcate the situation

- WL can probe unbiased power spectrum and higher order correaltion functions.
- It can probe non-linear scales.
- It can break Ω_m - σ_8 degeneracy.

- It can give clues to gas -dynamics in cluster physics when analysed with SZ.
- It can give provide information regarding bias when analysed jointly with Galaxy surveys.
- With tomographic and inversion techniques it can produce 3D dark maps.
- Weak lensing of CMB and other diffuse components can also be compared.
- Weak lensing of SN should be understood and can be exploted for cosmological information.

Table 1: List of forthcoming lensing surveys (adapted from Peacock et al. 2006). Surveys are sorted in three groups separated by a line. The top group show the current lensing surveys, the middle group shows survey starting in one year at the latest, and the group at the bottom is essentially not funded or partially funded projects.

Survey	Telescope	Sky coverage	Filters	depth
Deep Lens Survey	CTIO	7x4 deg^2	BVRz'	R=25
CFHTLS-Wide	CFHT	170 deg^2	ugriz	i_{AB}=24.5
RCS2	CFHT	1000 deg^2	grz	i_{AB}=22.5
KIDS	VST	1500 deg^2	ugriz	i_{AB}=22.9
Pan-STARRS	PS1	30000 deg^2	grizy	i_{AB}=24
VIKING	VISTA	1500 deg^2	zYJHK	i_{AB}=22.9
Dark Energy Survey	CTIO	5000 deg^2	griz	i_{AB}=24.5
DarkCam	VISTA	10000 deg^2	ugriz	i_{AB}=24
HyperCam	SUBARU	3500 deg^2	TBD	TBD
SNAP	Space	300/2000 deg^2	Narrow band (0.35-1.6)	TBD
LSST	6m ground	20000 deg^2	Narrow band (0.35-1.2)	i_{AB}=27
DUNE	Space	20000 deg^2	TBD	i_{AB}=25.5

-

Figure 27: DE Debate: Fundamentalist physics: why Dark Energy is bad for Astronomy http://arxiv.org/abs/0704.2291

Figure 28: DE Debate: A Thousand Invisible Cords Binding Astronomy and High-Energy Physics http://arxiv.org/abs/0708.1199